Earth Syst. Sci. Data, 9, 415–434, 2017
https://doi.org/10.5194/essd-9-415-2017

Open Access Earth System Science Data

The MSG-SEVIRI-based cloud property data record CLAAS-2

Nikos Benas[1], Stephan Finkensieper[2], Martin Stengel[2], Gerd-Jan van Zadelhoff[1], Timo Hanschmann[2], Rainer Hollmann[2], and Jan Fokke Meirink[1]

[1]Royal Netherlands Meteorological Institute (KNMI), De Bilt, the Netherlands
[2]Deutscher Wetterdienst (DWD), Offenbach, Germany

Correspondence to: Nikos Benas (benas@knmi.nl)

Received: 8 February 2017 – Discussion started: 28 February 2017
Revised: 31 May 2017 – Accepted: 2 June 2017 – Published: 10 July 2017

Abstract. Clouds play a central role in the Earth's atmosphere, and satellite observations are crucial for monitoring clouds and understanding their impact on the energy budget and water cycle. Within the European Organisation for the Exploitation of Meteorological Satellites (EUMETSAT) Satellite Application Facility on Climate Monitoring (CM SAF), a new cloud property data record was derived from geostationary Meteosat Spinning Enhanced Visible and Infrared Imager (SEVIRI) measurements for the time frame 2004–2015. The resulting CLAAS-2 (CLoud property dAtAset using SEVIRI, Edition 2) data record is publicly available via the CM SAF website (https://doi.org/10.5676/EUM_SAF_CM/CLAAS/V002). In this paper we present an extensive evaluation of the CLAAS-2 cloud products, which include cloud fractional coverage, thermodynamic phase, cloud top properties, liquid/ice cloud water path and corresponding optical thickness and particle effective radius. Data validation and comparisons were performed on both level 2 (native SEVIRI grid and repeat cycle) and level 3 (daily and monthly averages and histograms) with reference datasets derived from lidar, microwave and passive imager measurements. The evaluation results show very good overall agreement with matching spatial distributions and temporal variability and small biases attributed mainly to differences in sensor characteristics, retrieval approaches, spatial and temporal samplings and viewing geometries. No major discrepancies were found. Underpinned by the good evaluation results, CLAAS-2 demonstrates that it is fit for the envisaged applications, such as process studies of the diurnal cycle of clouds and the evaluation of regional climate models. The data record is planned to be extended and updated in the future.

1 Introduction

Clouds are of central importance for the Earth's energy budget and water cycle in modulating radiative fluxes and redistributing water. Consistent and stable observational data records of cloud properties are needed for climate monitoring and evaluating the distribution of clouds in weather and climate models. This requirement is reflected in the Intergovernmental Panel on Climate Change (IPCC)[1] statement that "clouds and aerosols continue to contribute the largest uncertainty to estimates and interpretations of the Earth's changing energy budget" (Stocker et al., 2013, chap. 7).

Passive visible–infrared (VIS–IR) imagers provide a valuable means to observe cloud properties with high spatial resolution. The long history of such instruments has enabled the generation of cloud data records. These include the International Satellite Cloud Climatology Project (ISCCP; Rossow and Schiffer, 1999), which is based on a combination of polar and geostationary imagers, the Pathfinder Atmospheres-Extended (PATMOS-x) data record, which is based on Advanced Very High-Resolution Radiometer (AVHRR) measurements (Heidinger et al., 2014), datasets derived from the Moderate Resolution Imaging Spectroradiometer (MODIS; Platnick et al., 2003) and the AVHRR-based cloud, albedo and radiation (CLARA) data record (Karlsson et al., 2013)

[1]a list of abbreviations is provided in Appendix A

created within the framework of the European Organisation for the Exploitation of Meteorological Satellites (EUMETSAT) Satellite Application Facility on Climate Monitoring (CM SAF; Schulz et al., 2009), which was recently updated (Karlsson et al., 2017).

While these datasets have global coverage, they give (apart from ISCCP) only a limited description of the temporal variability in clouds during the day. Therefore, CM SAF has been using measurements from the Spinning Enhanced Visible and Infrared Imager (SEVIRI), which is onboard the geostationary Meteosat Second Generation (MSG) satellites, to generate the CLoud property dAtAset using SEVIRI (CLAAS) with diurnally resolved cloud properties. The first edition of this data record (CLAAS-1) is described in Stengel et al. (2014). This dataset has been used to study the diurnal cycle of clouds (e.g., Martins et al., 2016; Pfeifroth et al., 2016) and for model evaluation (e.g., Brisson et al., 2016; Alexandri et al., 2015). Recently a second reprocessed edition was released (CLAAS-2, Finkensieper et al., 2016) based on updated retrieval algorithms and incorporating measurements from MSG-1, 2 and 3 satellites every 15 min, thus extending the time period covered (2004–2015) and increasing the temporal resolution. In particular, the 15 min resolution now enables process studies in which individual clouds or cloud fields need to be tracked to monitor cloud properties, such as glaciation.

In this study, the CLAAS-2 cloud properties are presented and evaluated. The data record is comprised of cloud macrophysical and microphysical properties, namely cloud fractional coverage (CFC; derived from a corresponding cloud mask), cloud phase (CPH), which distinguishes liquid and ice clouds, cloud water path (CWP) separately for liquid (LWP) and ice (IWP) clouds and cloud top location including height (CTH), pressure (CTP) and temperature (CTT). Cloud optical thickness (COT) and particle effective radius (REF), which are used in the cloud water path computation, are also included. All of these properties are available as both instantaneous data (level 2) and daily and monthly averages (level 3) along with monthly mean diurnal cycles and histograms.

The evaluation is performed by validation and intercomparison with other cloud datasets. These include (1) observations from space-based active instruments (lidar and radar), which provide the most accurate information about cloud presence in the atmosphere, (2) cloud properties derived from other passive VIS–IR satellite imagers, (3) observations of total cloud cover made at meteorological surface stations and (4) the liquid water path retrieved from spaceborne passive microwave (MW) sensors. The evaluation is performed separately for level 2 and level 3 CLAAS-2 data, and their performance is assessed based on the different characteristics of each dataset used as a reference. Consequently, depending on the parameter being evaluated, the analysis ranges from cloud detection scores and biases to spatial distribution characteristics and time series comparisons.

This paper is organized as follows: in Sect. 2 the satellite data and algorithms used to generate the CLAAS-2 data record are described; details on the data record contents are also provided. Datasets used for the evaluation of CLAAS-2 are introduced in Sect. 3 along with the methodology used in each case. In Sect. 4 evaluation results regarding level 2 data are presented, while the corresponding results for monthly aggregated (level 3) products are described in Sect. 5. Concluding remarks can be found in Sect. 6.

2 The CLAAS-2 data record

2.1 SEVIRI

SEVIRI is a 12-channel imager on the MSG geostationary satellites operated by EUMETSAT. All four planned MSG satellites, Meteosat-8, 9, 10 and 11, (also referred to as MSG-1, 2, 3 and 4, respectively), have been launched. Data from the first three satellites are included in the CLAAS-2 data record covering the period from January 2004 to December 2015. Apart from one high spatial resolution visible (HRV) channel, SEVIRI carries 11 channels between 0.6 and 14 µm with a spatial sampling resolution of 3×3 km at nadir and a 15 min repeat cycle. Further information regarding the SEVIRI channels is given in Table B1 of Appendix B. The MSG satellites have been located at similar but not exactly the same positions. Specifically, MSG-1 was positioned at 3.4° E from 2004 to 2008. Hence, even though the SEVIRI projection in level 1.5 data is aligned at 0.0° for all satellites, the positions of the individual satellites slightly change the SEVIRI viewing geometries, which has been taken into account for the generation of the CLAAS-2 data record.

In addition to the EUMETSAT nominal calibration, SEVIRI solar channels were intercalibrated with MODIS operating onboard the Aqua satellite, which is considered one of the best-calibrated imagers at present (Wu et al., 2013). The methodology of Meirink et al. (2013), which uses collocated, ray-matched, atmosphere-corrected, near-nadir SEVIRI and Aqua MODIS reflectances, was reapplied for our study using MODIS Collection 6 level 1b data as a reference and extended to cover the full CLAAS-2 time series. This included all three SEVIRI instruments that have been active on MSG-1, 2 and 3. The inter-calibration with MODIS changed the reflectances by about −8 % in channel 1 (0.6 µm), −6 % (−4 % for MSG-3) in channel 2 (0.8 µm) and +3 % in channel 3 (1.6 µm) compared to the operational SEVIRI calibration provided by EUMETSAT. Furthermore, even though the SEVIRI shortwave channels turn out to be quite stable over time, there are slight trends in the calibration coefficients. The calibration coefficients used in CLAAS-2 are reported in CM SAF (2016a). For the thermal infrared channels, the onboard calibration as provided by EUMETSAT was applied.

2.2 CLAAS-2

The CLAAS-2 dataset is the improved and extended follow-up to CLAAS-1 (Stengel et al., 2014). In the following, an overview of each CLAAS-2 retrieval algorithm is given, along with the main scientific updates applied, compared to the CLAAS-1 retrievals.

For the detection of clouds and their vertical placement, the MSGv2012 software package developed within the framework of the Nowcasting and Very Short Range Forecasting SAF (NWC SAF) was employed. Cloud detection involves a series of spectral threshold tests depending on the illumination (daytime, twilight, nighttime, sun glint) and surface types among other factors. The algorithm classifies satellite pixels as cloud filled, cloud free, cloud contaminated or snow/ice contaminated. Further information on the cloud detection method can be found in Derrien and Le Gléau (2005), NWC SAF (2013) and Stengel et al. (2014) regarding its implementation in CLAAS-1. Compared to the MSGv2010 algorithm version, which was applied in CLAAS-1, only minor updates were implemented. These include adaptations of detection tests that were affected by nocturnal extreme cooling conditions, which caused false cloud detections by the algorithm (NWC SAF, 2011), and corrections for coastal cloud mask artifacts caused by high spatial standard deviation values around coastal pixels (CM SAF, 2016a). Furthermore, contrary to the default NWC SAF MSGv2012 cloud masking algorithm, which uses 4×4 pixel segments to reduce computational time, individual thresholds were computed for each SEVIRI pixel in CLAAS-2. The consequent increase in the CLAAS-2 computation time was compensated for by a higher degree of parallelization.

Regarding the cloud vertical placement algorithm, no changes were implemented between the CLAAS-1 (MSGv2010) and CLAAS-2 (MSGv2012) versions. The algorithm, which is used for the derivation of CTH, CTP and CTT, uses input from SEVIRI channels at 6.2, 7.3, 10.8, 12.0 and 13.4 µm. The spectral information is used in the simulation of corresponding radiances and brightness temperatures for overcast and clear sky conditions on a pixel basis, using the Radiative Transfer for TOVS (RTTOV; Saunders et al., 1999; Matricardi et al., 2004). Ancillary data for temperature and humidity profiles from ERA-Interim are also used (Dee et al., 2011). Different approaches are used for the derivation of CTP, including a best fit between the simulated and the measured 10.8 µm brightness temperatures, the H2O–IRW (infrared window) intercept method (Schmetz et al., 1993) and the radiance rationing method (Menzel et al., 1983). Further information on the implementation of the retrieval algorithm for cloud top properties can be found in Stengel et al. (2014) and CM SAF (2016a).

The retrieval of CPH in CLAAS-2 was based on a modified version of the Pavolonis et al. (2005) algorithm, which was provided by the Center for Satellite Applications and Research (STAR) of the NOAA Satellite and Information Service (NESDIS). This approach constitutes a fundamental update compared to CLAAS-1, for which CPH was mainly inferred from CTT and the 1.6 µm reflectance. According to the new retrieval scheme, a number of spectral tests are performed in a specific order involving measurements from SEVIRI channels at 6.2, 8.7, 10.8, 12.0 and 13.4 µm, as well as clear and cloudy sky IR radiances and brightness temperatures calculated using RTTOV. The algorithm initially yields one of the following cloud types: liquid, supercooled, opaque ice, cirrus, overlap or overshooting, which are then further condensed to liquid (former two) and ice (latter four) phase. Details on the algorithm can be found in CM SAF (2016b).

The retrieval of cloud optical and microphysical properties was based on the Cloud Physical Properties (CPP) algorithm (Roebeling et al., 2006; CM SAF, 2016b). The algorithm uses SEVIRI visible (0.6 µm) and near-infrared (1.6 µm) measurements to retrieve COT and REF by applying the classical Nakajima and King (1990) approach. CPP is based on lookup tables (LUTs) of top-of-atmosphere (TOA) reflectances simulated by the Doubling–Adding KNMI (DAK) radiative transfer model (Stammes, 2001), which has been frequently used in the past for numerous cloud and aerosol radiative transfer applications (e.g., de Graaf et al., 2012; Tilstra et al., 2012). The setup of these LUTs is provided in Table 1, which also contains information on the underlying single-scattering calculations for liquid and ice cloud particles, as well as information on the assumed shape and properties of ice particles. Absorption by atmospheric trace gases is taken into account based on Moderate Resolution Atmospheric Transmission (MODTRAN4 version 2; Anderson et al., 2001) simulations. LWP and IWP are calculated following Stephens (1978):

$$\mathrm{LWP} = \frac{2}{3}\rho_{\mathrm{l}} r_{\mathrm{e}} \tau, \quad \mathrm{IWP} = \frac{2}{3}\rho_{\mathrm{i}} r_{\mathrm{e}} \tau, \tag{1}$$

where ρ_{l} and ρ_{i} are the densities of water and ice, respectively, r_{e} is REF and τ is COT. No retrievals are performed for solar zenith angles (SZAs) or viewing zenith angles (VZAs) larger than 84° due to high uncertainties in the retrieved properties at these angles. The main updates of CPP compared to CLAAS-1 include the generation of new LUTs with an extension in the range of SZAs and VZAs, the number and range of REF and the inclusion of observational sea ice (OSI SAF, 2016) and ERA-Interim snow cover data to better characterize the surface albedo, which for all other surface types is taken from MODIS (Moody et al., 2005).

CLAAS-2 level 2 data contain 15 min SEVIRI pixel-based retrievals from 2004 to 2015. Level 3 data contain daily and monthly aggregated products. For the cloud parameters considered here, the daily aggregation was done by linear averaging all valid retrievals (available on the native SEVIRI projection) into $0.05° \times 0.05°$ grid boxes. Daily means were then further averaged to monthly means; at least 20 daily mean values were required for the estimation of the monthly average CFC. It should be noted, however, that this

Table 1. Specification for the LUTs created with DAK. Discrete values are given for all variables spanning the axes of the LUTs.

Variable	range	number of points
cos(SZA)	0.099–1 (SZA: 0–84.3°)	73, Gauss points
cos(VZA)	Same as cos(SZA)	Same as cos(SZA)
Relative azimuth angle	0–180°	91, equidistant
COT	0 and 0.25–256	22, equidistant in log(COT)
REF liquid[a]	3–34 µm	8, equidistant in log(REF)
REF ice[b]	5–80 µm	9, equidistant in log(REF)

[a] Single-scattering properties have been calculated using Mie theory for spherical droplets with a two-parameter gamma size distribution (effective variance = 0.15) and complex refractive index from Segelstein (1981). [b] Single-scattering properties have been calculated using ray tracing for randomly oriented monodisperse imperfect hexagonal ice crystals (Hess et al., 1998) with aspect ratios from Yang et al. (2013), roughening simulated with a distortion angle of 30° and a complex refractive index from Warren and Brandt (2008). The choice of this ice particle model is motivated by Knap et al. (2005) who showed that it yields adequate simulations of total and polarized ice cloud reflectances observed by the Polarization and Directionality of the Earth's Reflectances (POLDER) instrument.

threshold was only applied as a fail-safe mechanism; in practice, apart from the first month of the CLAAS-2 time series (January 2004), no gaps are present in the monthly mean data. CFC was calculated from the cloud mask by counting cloud-free pixels as 0 and both cloud-contaminated and cloud-filled pixels as 1. In addition to the "day and night" CFC, separate averages for daytime and nighttime were computed. Level 3 products of cloud LWP and IWP (including COT and REF) are available during daytime only, both as cloudy-sky means and all-sky means. Apart from the regular monthly aggregated products, monthly mean diurnal cycles have been calculated by averaging all daily mean diurnal cycles in a month. In order to retain a sufficient number of observations in each grid box, these monthly mean diurnal cycles have been prepared on a coarser spatial grid of $0.25° \times 0.25°$. In addition to the mean monthly properties, monthly histograms are composed by collecting the number of occurrences of cloud properties. These are CWP, CTP, CTT, COT and REF in one-dimensional, cloud-phase-separated, spatially resolved histograms with $0.05° \times 0.05°$ of spatial resolution and combinations of CTP and COT in two-dimensional, cloud-phase-separated, spatially resolved histograms with $0.25° \times 0.25°$ of spatial resolution. The binning of the histograms is given in Table 3 following Stengel et al. (2014). The REF histograms, which were not included in CLAAS-1, have bin borders of 3, 6, 9, 12, 15, 20, 25, 30, 40, 60 and 80 µm.

The CLAAS-2 data record is (as all CM SAF climate data records) freely available online via https://doi.org/10.5676/EUM_SAF_CM/CLAAS/V002 and includes comprehensive documentation and auxiliary data to facilitate work with the data record. CM SAF's (www.cmsaf.eu) main task is to generate and provide climate data records (CDRs) derived from operational meteorological satellites. CDRs for components of the global energy budget and water cycle are the particular focus. During the full generation and delivery process, CM SAF adheres to the international Global Climate Observing System (GCOS) guidelines. Thus, CM SAF applies the highest standards to make the resulting data records suitable for the analysis of climate variability and the detection of climate trends.

3 Datasets and methodology used for evaluation

In this section, the datasets used as references for the evaluation of CLAAS-2 are described, along with the methodology used in each case. Reference datasets are comprised of measurements from lidar, radar, microwave and passive spaceborne sensors, as well as surface observations.

3.1 CALIOP

The Cloud-Aerosol Lidar with Orthogonal Polarization (CALIOP) is a lidar instrument onboard the CALIPSO (Cloud-Aerosol Lidar and Infrared Pathfinder Satellite Observation) satellite that has provided cloud and aerosol profile information since August 2006 (Winker et al., 2009). CALIOP products are retrieved based on backscattered signal at 1064 and 532 nm and are available at horizontal and vertical resolutions of 333 and 30–60 m, respectively. They include cloud phase and type for up to 10 cloud layers per column and CTP, CTH and CTT at each layer top.

The CALIOP level 2 layered cloud products (CAL_LID_L2_05kmCLay-Prov) with 5 km of resolution (dataset versions 3-01, 3-02 and 3-30) were used here. Among the five different CALIOP along-track resolutions available at 333 m, 1 km, 5 km, 20 km and 80 km, the 5 km resolution was selected as the closest to the CLAAS-2 level 2 resolution. It also offers higher confidence in cloud detection and identification compared to the original footprint resolution by horizontally averaging up to 80 km of measurements (Winker et al., 2009). For the CLAAS-2 level 2 validation, a dataset of collocated CALIOP and CLAAS-2 measurements was created and is comprised of 100 million matchups between 2006 and 2015. Spatial collocation was

Table 2. Contingency table for the CLAAS-2 and CALIOP observations; n is the number of cases and 1 and 2 correspond to clear or cloudy for the cloud mask and water or ice for the cloud phase.

	CALIOP reports 1	CALIOP reports 2
CLAAS-2 reports 1	n_{11}	n_{12}
CLAAS-2 reports 2	n_{21}	n_{22}

performed using a nearest neighbor approach while temporal collocation was achieved by matching each CALIOP measurement time with the acquisition time of the closest SEVIRI scanline. This approach allows for maximum time and space differences of 7.5 min and 5 km, respectively.

CLAAS-2 level 2 products were validated against corresponding CALIOP products (Sect. 4.1). For the discrete variables cloud mask (cloudy or clear) and CPH (water or ice), validation was based on statistical scores, including the probability of detection (POD), the false alarm ratio (FAR), the hit rate and the Hanssen–Kuiper skill score (KSS). Downscaled spatial distributions were also compared. The formulas used for the computation of these scores are the following:

$$\text{POD for event 1, 2}: \frac{n_{11}}{n_{11}+n_{21}}, \frac{n_{22}}{n_{22}+n_{12}}, \tag{2}$$

$$\text{FAR for event 1, 2}: \frac{n_{12}}{n_{11}+n_{12}}, \frac{n_{21}}{n_{22}+n_{21}}, \tag{3}$$

$$\text{Hit rate}: \frac{n_{11}+n_{22}}{n_{11}+n_{12}+n_{21}+n_{22}}, \tag{4}$$

$$\text{KSS}: \frac{n_{11}n_{22}-n_{21}n_{12}}{(n_{11}+n_{21})(n_{12}+n_{22})}. \tag{5}$$

In the above formulas, n_{ij} is the number of cases for which CLAAS-2 reports event i and CALIOP reports event j (Table 2). Events correspond to cloudy and clear cases for cloud mask and water or ice clouds for CPH.

It should finally be noted that CALIOP's higher sensitivity to high and optically thin clouds, compared to SEVIRI, is an important factor affecting the validation results. In order to address this sensitivity difference and investigate the accuracy of CLAAS-2 products, comparisons were repeated by sampling the CALIOP profiles at successive layers below the cloud top using different thresholds for the integrated COT of these layers.

3.2 DARDAR

The DARDAR (lidar–radar) dataset was created using a synergistic approach that combines data from the Cloudsat Cloud Profiling Radar (CPR) on reflectivity, CALIOP lidar attenuated backscatter and MODIS infrared radiance measurements to retrieve the ice cloud properties COT, REF and IWP. The retrieval is based on an optimal estimation approach, which ensures a smooth transition between regimes for which different instruments are sensitive (Delanoë and Hogan, 2008, 2010). The products have the same vertical resolution as CALIOP (30–60 m) and the horizontal resolution of CPR (700 × 700 m).

DARDAR data for ice COT and IWP were used for the validation of corresponding CLAAS-2 level 2 products. The DARDAR data used here are comprised of overpasses from the SEVIRI disk during January and July 2008. Extreme illumination geometries were excluded by selecting only retrievals at SZAs below 75°. Furthermore, DARDAR profiles that consist only of ice CPH were considered, and in each SEVIRI pixel a single profile was included only when all profiles in this pixel had the same CPH.

3.3 MODIS

MODIS is an advanced imaging spectroradiometer operating onboard the NASA Terra and Aqua satellites since February 2000 and July 2002, respectively (Salomonson et al., 1989). Both the Terra and Aqua orbits are sun synchronous and timed so that they cross the equator at 10:30 and 13:30 local solar times in a descending and ascending node, respectively. With a viewing swath width of 2330 km, MODIS covers every point on the Earth's surface in 1 to 2 days, acquiring data in 36 spectral bands.

Since MODIS is among the most advanced passive imagers in space and has been operating during the entire CLAAS-2 time range, cloud products from the latest MODIS collection (C006; Platnick et al., 2015) were used here as a reference. For level 2 intercomparisons (Sect. 4.3), a specific MODIS granule was selected as a case study, and the MODIS and SEVIRI grids were sampled to a common regular latitude–longitude grid. For level 3 evaluation (Sect. 5.3), the CLAAS-2 monthly products were downscaled from their 0.05° × 0.05° resolution to the MODIS 1° × 1° grid by spatial averaging. Since both level 2 and 3 MODIS data products are available separately from Terra and Aqua satellites and CLAAS-2 level 3 monthly mean products are computed by averaging all SEVIRI time slots (only daytime slots for optical properties), Terra and Aqua MODIS monthly products were also averaged to best mimic this CLAAS-2 diurnal averaging. In the CFC and CPH cases, however, only Aqua MODIS data were used due to a Terra MODIS band 29 (8.6 µm) radiometric calibration drift issue, which has affected Collection 6. This band is used in the CFC and CPH retrieval algorithms (Baum et al., 2012) in which significant biases were found in the monthly time series extending back to earlier than 2010. As in the optical properties case, only daytime CFC and CPH data were compared against MODIS. It should also be noted that, for consistency, cloud optical property retrievals based on MODIS band 6 (1.6 µm) were used in these intercomparisons.

Table 3. Validation results for CLAAS-2 level 2 cloud mask (CMa) and cloud phase (CPH).

		CALIOP ICOT > 0.0					CALIOP ICOT > 0.2				
		All	Day	Night	Sea	Land	All	Day	Night	Sea	Land
CMa	POD clear	69.4	67.1	71.9	58.0	88.0	61.4	58.3	64.9	49.6	80.6
	FAR clear	23.6	20.7	26.4	18.6	28.2	5.5	3.4	7.5	2.9	7.9
	POD cloudy	87.5	88.7	86.5	93.1	75.2	96.2	97.5	95.2	98.6	90.3
	FAR cloudy	16.9	19.3	14.6	19.1	10.2	29.8	34.3	25.3	31.9	23.1
	Hit rate	80.9	80.3	81.5	81.1	80.6	78.3	75.9	80.7	75.1	84.6
	KSS	56.9	55.9	58.4	51.1	63.2	57.6	55.8	60.1	48.3	70.9
CPH	POD liquid	91.6	89.3	93.7	92.9	84.7	85.5	83.7	87.0	88.0	74.8
	FAR liquid	29.8	27.3	31.9	25.2	48.2	10.0	9.8	10.2	7.6	20.1
	POD ice	74.9	77.9	72.3	73.6	77.3	88.9	90.1	87.7	89.1	88.4
	FAR ice	6.7	8.3	5.2	7.5	5.4	16.0	16.4	15.6	16.7	14.9
	Hit rate	81.4	82.4	80.6	82.4	79.0	87.0	86.8	87.3	88.5	83.2
	KSS	66.5	67.2	66.0	66.5	62.0	74.4	73.8	74.7	77.2	63.2

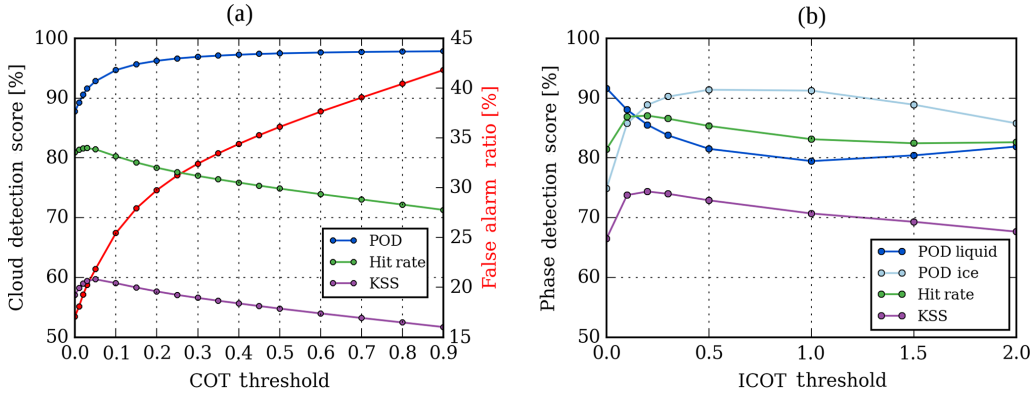

Figure 1. **(a)** CLAAS-2 cloud detection scores as a function of the COT threshold used to discriminate clear and cloudy CALIOP observations. KSS denotes the Hanssen–Kuiper skill score. **(b)** CLAAS-2 cloud phase detection scores as a function of the integrated COT (ICOT) threshold, which determines the reference cloud layer.

3.4 SYNOP

Total cloud cover data from surface synoptic observations (SYNOP) were used for the evaluation of CLAAS-2 level 3 monthly CFC. SYNOP data span the entire CLAAS-2 period (2004–2015) and originate from all land areas of the SEVIRI disk, with a higher density of stations in European countries. The SYNOP data used for the validation have been taken from the local DWD archive of collected global SYNOP reports following the guidance of the Guide to Meteorological Instruments and Methods of Observations (Jarraud, 2008). In order to ensure data quality and consistency, only SYNOP reports provided by manned airport stations were taken into account.

Monthly averaged CFC values from SYNOP stations were estimated based on corresponding daily averages. The latter were calculated when at least six instantaneous measurements were available. Additionally, as in the CLAAS-2 level 3 case, at least 20 daily mean CFC values were required for the estimation of monthly averages. Except for the level of agreement between the SYNOP and collocated CLAAS-2 level 3 CFC products, the dependency of this agreement on the SEVIRI VZA was also examined (Sect. 5.1).

3.5 Microwave imagers

MW-based retrievals from the University of Wisconsin (UWisc) LWP climatology were used for the validation of CLAAS-2 level 3 LWP. This dataset, described in detail in O'Dell et al. (2008), was created based on retrievals from various MW sensors, including the Special Sensor Microwave Imager (SSM/I), the Tropical Rainfall Measuring Mission (TRMM) and the Advanced Microwave Scanning Radiometer for Earth Observing System (AMSR-E). The UWisc dataset provides monthly mean diurnal cycles over global oceans at $1° \times 1°$ of spatial resolution during 1988–2008. LWP estimates are reported to have an accuracy of 15 to 30 % (O'Dell et al., 2008).

It should be noted that, since MW measurements are not sensitive to the presence of ice clouds, the validation was limited to areas with a sufficiently low ice cloud fraction. In the SEVIRI disk this requirement is fulfilled over the marine stratocumulus (Sc) area of the southern Atlantic off the Namibian coast. Specifically, the region defined by the 20–10° S and 0–10° E latitude–longitude boundaries was selected for this purpose. Validation includes both monthly mean time series and average diurnal cycle intercomparisons of all-sky LWP computed by averaging pixel values from the Sc study region (Sect. 5.2).

4 Level 2 evaluation

In this section, the validation results of CLAAS-2 level 2 products against CALIOP and DARDAR are described. We also discuss comparisons of CLAAS-2 level 2 products with MODIS data.

4.1 Validation with CALIOP

Based on all collected CLAAS-2 level 2 and CALIOP collocations, an overall cloud POD of 87.5 % was found, while the corresponding FAR was 16.9 % and the hit rate reached 80.9 %. Differences between day and night collocations were minor; the cloud POD was significantly higher over sea compared to land at the cost of an also much higher FAR.

The corresponding scores for CPH were 91.6 and 74.9 % (liquid and ice POD) and 29.8 and 6.7 % (liquid and ice FAR) with an overall CPH hit rate of 81.4 %. Both low values of ice cloud POD and high values of liquid cloud FAR should be attributed to CALIOP's higher sensitivity to high and optically thin clouds. In fact, when these clouds are excluded from the analysis, ice cloud scores acquire higher values with ice POD becoming similar to the liquid POD, while liquid cloud FAR is reduced to 10.0 % when the CALIOP phase was sampled at a COT of 0.2 below the cloud top. These results are summarized in Table 3.

This difference in sensitivity between CLAAS-2 and CALIOP was further analyzed using a varying CALIOP total column COT as a threshold for distinguishing cloud-free from cloudy scenes. Hence, all CALIOP scenes with a COT of less than this threshold were set as cloud free. Results are shown in Fig. 1a with the COT threshold on the x axis. It is clear that as the COT threshold used to distinguish clear and cloudy CALIOP measurements increases, both POD and FAR increase. The POD increases because optically thin clouds, which are likely not to be detected by SEVIRI, are also excluded from CALIOP and the number of scenes in which both CALIOP and CLAAS-2 detect clouds increases. However, as the COT threshold increases, some clouds that are detected by SEVIRI are also excluded from CALIOP; such cases cause an increase in FAR. These combined effects cause the hit rate and KSS to peak at COT ≈ 0.05.

The effect of using the CALIOP CPH for the layer at which the integrated COT (ICOT) exceeds a certain threshold instead of the uppermost layer is shown in Fig. 1b. Applying this ICOT threshold leads to an increase in ice cloud POD, since thin ice clouds detected by CALIOP but not by SEVIRI are excluded. There are two ways the liquid POD can be influenced when excluding a thin CALIOP ice cloud and instead comparing against a liquid CALIOP cloud located below. If the thin ice cloud was incorrectly reported as liquid by CLAAS-2, the liquid POD would increase; it would decrease if the cloud was correctly reported as ice by CLAAS-2. It was found that occurrences of the second case increased with ICOT 3 times more than the first, leading to the decrease in liquid cloud POD shown in Fig. 1b.

Figure 2 shows the spatial distributions of the cloud fraction and the ice cloud fraction estimated from all collocated CLAAS-2 level 2 and CALIOP measurements. The maps were created by remapping matchups to a regular $1.5° \times 1.5°$ grid and averaging within each grid box. Large-scale patterns between the two datasets are similar for both the cloud fraction and phase. There is a tendency for CLAAS-2 to overestimate cloud fraction over the northern and southern Atlantic as well as the Indian Ocean, which may be related to the high VZAs over these areas (Reuter et al., 2009). On the other hand, the cloud fraction in the tropics is underestimated by CLAAS-2, probably due to the frequent presence of cirrus clouds in this area, which are more likely to be detected by CALIOP (Sun et al., 2011). The phase agreement is very good overall, with slightly fewer ice clouds reported by CLAAS-2 over Africa and the central Atlantic, which is consistent with the difference in the cloud fraction over the same areas.

Taking the CALIOP CTT as a reference, the relation of CTT and CPH was also examined (Fig. 3). The agreement is excellent in both liquid and ice cloud histograms when using ICOT $= 0.2$ as a threshold layer for CALIOP CTT and CPH selection. It should be noted that the CLAAS-2 histogram extensions above 0 °C for ice clouds (red dashed line in Fig. 3) and below −42 °C for liquid clouds (red solid line in Fig. 3) should be attributed to the fact that the x axis CTT binning in this figure comes from CALIOP. The CLAAS-2 CTT is always below 0 °C for ice clouds and above −42 °C for liquid clouds. Hence, these histogram extensions are related to CALIOP retrieving higher CTT (former case) or lower CTT (latter case) than CLAAS-2. If CLAAS-2 CTT was used instead, such cases would not be allowed by the retrieval algorithm.

The CLAAS-2 cloud top properties, namely CTH, CTP and CTT, were directly compared to corresponding CALIOP data for the uppermost cloud layer detected. These comparisons revealed an underestimation of CTH by CLAAS-2 and consequent overestimations of CTP and CTT. These results should also be attributed to the discrepancies in high optically thin cloud detection between the two datasets. In fact, when examining these biases using varying CALIOP cloud

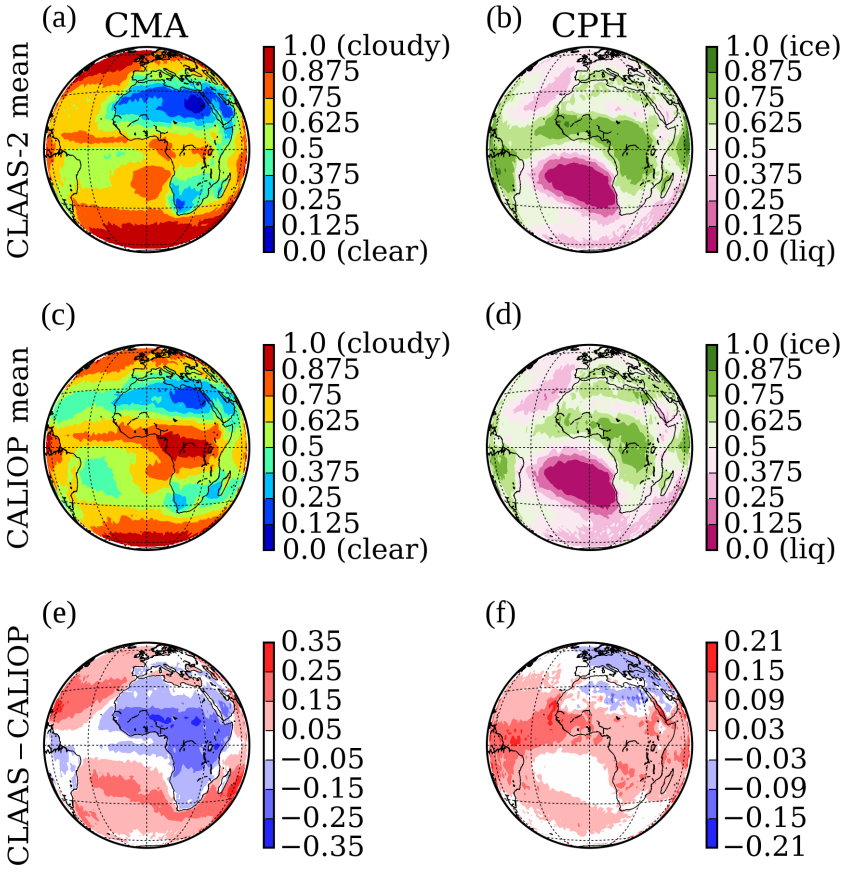

Figure 2. Spatial distribution of the cloud fraction from CLAAS-2 level 2 **(a)** and CALIOP **(c)** and the fraction of ice clouds (**b** and **d**). The bottom row shows the absolute difference in CLAAS and CALIOP for the cloud fraction **(e)** and the fraction of ice clouds **(f)**. Note the different scaling in **(e)** and **(f)**. The CALIOP cloud detection criterion is total column COT > 0, while the CALIOP phase is taken from the layer at which ICOT exceeds 0.2.

top layers based on different ICOT threshold values, a strong influence was found (Fig. 4). All biases acquire their minimum absolute values at an ICOT threshold of about 0.3–0.5 and their signs are reversed as the ICOT of CALIOP excluded cloud top layers increased towards 2.0. The spread of CLAAS-2 compared to CALIOP data is also reduced, as can be seen from the bias-corrected root mean square error (bc-RMSE) represented as error bars in Fig. 4.

In contrast to level 2 cloud mask and cloud phase variables, which acquire values of only 0 or 1, cloud top variables are continuous so that a correlation analysis can be performed. The results are shown as scatterplots in Fig. 5. The overall correlation is strong in all cloud top products, with Pearson correlation coefficients ranging between 0.84 and 0.88. The least-squares fit slopes are below 1, which also reflects the underestimation in CTH and overestimation in CTP and CTT of high clouds by CLAAS-2.

4.2 Validation with DARDAR

Figure 6a shows the CLAAS-2 versus DARDAR ice COT comparison. The distribution contours show the number of points enclosed, e.g., the black area (central contour) encloses the 20 % of bins containing the largest density of observations. The distribution is clearly correlated and lies along the 1 : 1 line. However, the remaining 25 % of the observations outside of the density contours (not shown in the figure) are so scattered that the total correlation remains weak (0.33).

The IWP (Fig. 6b) is proportional to the product of ice COT and REF, as expressed in Eq. (1). Hence, the transition of the ice COT correspondence along the 1 : 1 line (Fig. 6a) into the curved IWP distribution in Fig. 6b should be attributed to differences in ice REF. This curved distribution for low IWP values also appears in the results of Eliasson et al. (2013), in which IWP from MODIS and PATMOS-x is compared with DARDAR. Figure 6c shows that the range of IWP values and the distribution of occurrences in this range are similar between DARDAR and CLAAS-2.

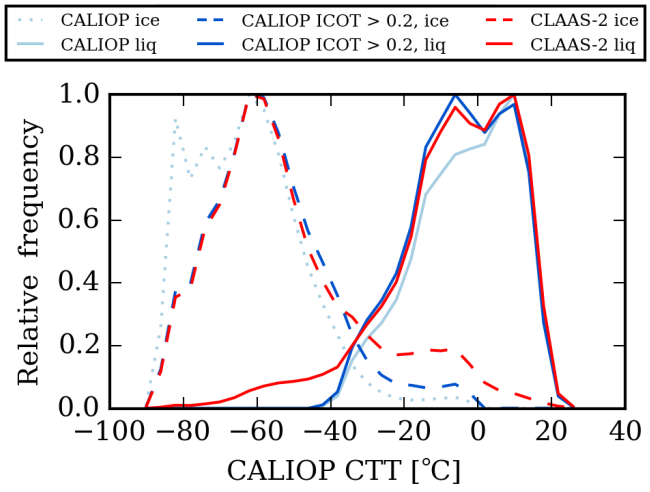

Figure 3. Phase histograms for liquid and ice clouds as a function of CALIOP cloud top temperature. For the red and blue lines, binning is based on the CALIOP CTT taken from the layer at which ICOT exceeds 0.2. For the light blue line, the phase and temperature of the uppermost CALIOP cloud layer were used. Bin size is 4 °C.

These results highlight the difficulty in interpreting an evaluation of passive versus active instruments. The main reasons for this difficulty include the different microphysical assumptions applied in the retrievals and the difference between column-averaged (but weighted to the top of the cloud) retrievals from variable viewing geometries for the passive instrument versus profile information from a near-nadir view for the active instruments.

4.3 Comparison with MODIS

For the level 2 CLAAS-2 comparison with MODIS Collection 6, one Terra MODIS granule is shown as a case study. The granule on 20 June 2008 from 10:50 to 10:55 UTC, covering the largest part of Europe, was selected because it fulfilled a number of criteria, including a balanced presence between low and high, liquid and ice and thin and thick clouds, as well as relatively low SZAs. The time difference between the two datasets was also minimized by selecting the 10:45 UTC SEVIRI time slot, which covered Europe at around 10:56 UTC.

Figure 7 shows histograms of CLAAS-2 and MODIS COT, REF and CWP from this granule separately for liquid and ice clouds, created using only collocations for which CPH was the same in both datasets. The liquid COT histograms reveal good agreement, while ice COT is slightly larger in CLAAS-2 than in MODIS. Relative peaks at COT = 100 should be attributed to the fact that COT retrievals greater than 100 are set equal to 100, causing the relatively higher number of pixels found with this value. The MODIS 1.6 and 2.1 µm REF retrievals yield slightly different histograms. Considering that the CLAAS-2 products are based on 1.6 µm measurements, it is somewhat surprising that the CLAAS-2 REF agrees better with the MODIS 2.1 µm product than the 1.6 µm, especially in the liquid cloud case. For ice clouds, CLAAS-2 acquires an overall lower REF, which is most probably related to the choice of ice particle habits; i.e., the severely roughened monodisperse hexagonal columns for CLAAS-2 versus the severely roughened aggregated columns with a gamma size distribution (Yang et al., 2013) for MODIS C6. Consistent with the results of the REF intercomparison, the agreement for LWP is better than for IWP.

5 Level 3 evaluation

This section covers the evaluation of CLAAS-2 level-3 products for daily and monthly aggregations and monthly mean diurnal cycles.

5.1 Validation with SYNOP

The comparison of CLAAS-2 monthly mean CFC data with corresponding SYNOP observations showed overall good agreement with a CLAAS-2-SYNOP bias (over all SYNOP stations) of 3.7 % on average and a 7.5 % maximum. This bias, however, is positive for the entire time series as a consequence of the well-known effect of cloudiness overestimation by passive satellite sensors at high VZAs (e.g., Maddux et al., 2010) in combination with most SYNOP stations being located in central Europe, away from the SEVIRI nadir viewpoint.

This effect was verified by a more detailed analysis of the dependency of CFC bias on VZA. The results of this analysis are shown in Fig. 8, for which CFC bias values have been averaged in 10° VZA bins along with the bc-RMSE values, which gives a measure of the precision of CLAAS-2 observations, and the number of observations available from SYNOP. The bias is negative for VZAs below 40° and becomes positive for larger angles. While positive bias values are explained by the CFC overestimation of SEVIRI at high VZAs, negative values below 40° could be attributed to a similar local-scale effect from SYNOP, whereby ground-based observations tend to overestimate cloudiness (especially towards the horizon) compared to the low VZA retrievals from SEVIRI. This scenery effect leads to an overestimation of CFC by SYNOP due to the obscuring of cloud-free spaces by convective clouds with a high vertical extent (Karlsson, 2003). However, the small number of observations in this VZA range is prohibitive for drawing any further conclusions. In the 30–60° VZA range, on the other hand, the best accuracy and precision of CLAAS-2 CFC are achieved. The northern midlatitudes (i.e., Europe) dominate this VZA range where the greatest number of observations can also be found, thus enhancing the robustness of the results.

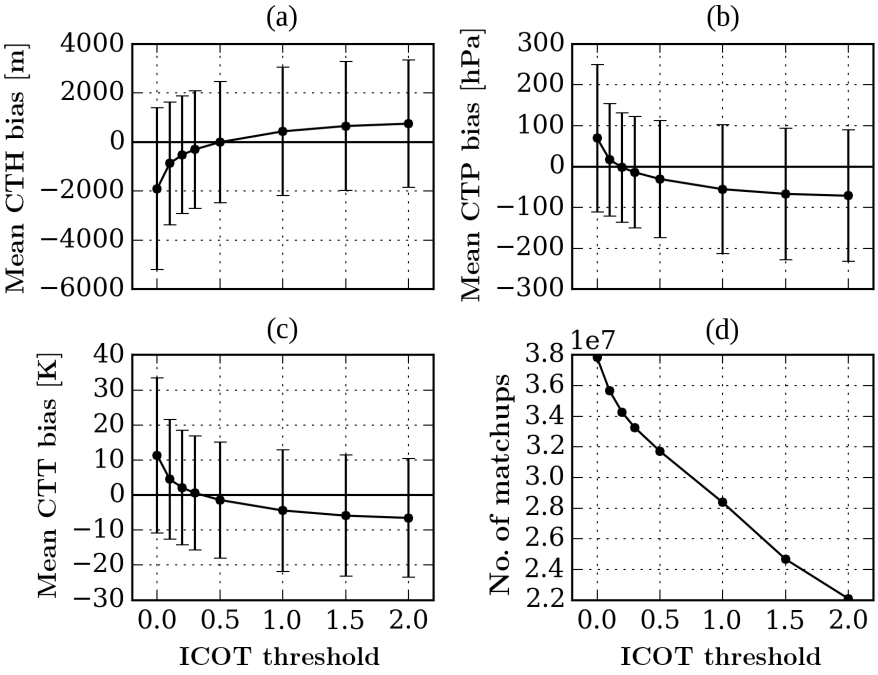

Figure 4. Mean biases (CLAAS-2–CALIOP) of CTH **(a)**, CTP **(b)** and CTT **(c)** compared against the CALIOP cloud layer at which ICOT exceeds a certain threshold. The error bars represent the bc-RMSE. The number of collocated measurements is also shown **(d)**.

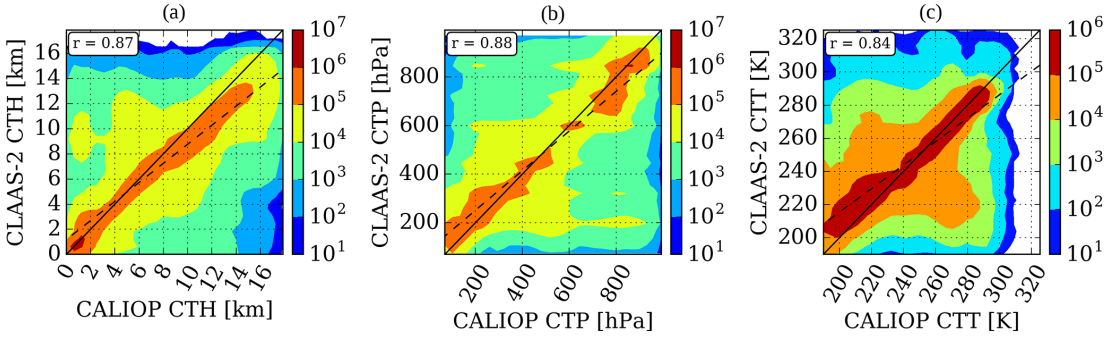

Figure 5. Scatterplots of cloud top products between CLAAS-2 and CALIOP: CTH **(a)**, CTP **(b)** and CTT **(c)**. The diagonal is marked by a solid line, and the dashed lines show the result of a least-squares linear fit. The text box in the upper left corner displays the Pearson correlation coefficient. The p values are practically zero because of the very large number of matchups. CALIOP values were taken from the layer at which ICOT exceeds 0.2 in all plots.

5.2 Validation with UWisc

Figure 9a shows the time series plot of the monthly all-sky LWP at 12:00 UTC from CLAAS-2 and UWisc, calculated over the marine Sc region west of Namibia (0–10° E, 10–20° S). The two data records exhibit similar seasonal characteristics, with the largest differences appearing almost every year in August and September when CLAAS-2 acquires lower values compared to the UWisc all-sky LWP. This characteristic should be attributed to the presence of absorbing aerosols over the clouds, originating from biomass burning activities during this season; these overlying aerosols cause a negative bias in the LWP retrieval (Haywood et al., 2004).

The average diurnal cycle of all-sky LWP over the marine Sc region from CLAAS-2 and UWisc is shown in Fig. 9b. In order to ensure the equivalence of the results, all spatial averages computed from cases with more than 50 % missing values were excluded from the analysis, leading to the absence of nighttime and twilight hours from the plot. Both CLAAS-2 and UWisc show the reduction in all-sky LWP throughout the day in the 10 h part of the diurnal cycle depicted in Fig. 9b. The smoothness of the UWisc curve should be attributed to its derivation as a fit to satellite data from various overpass times (O'Dell et al., 2008). Compared to UWisc, CLAAS-2 exhibits overall similar values, except before sunset, with an

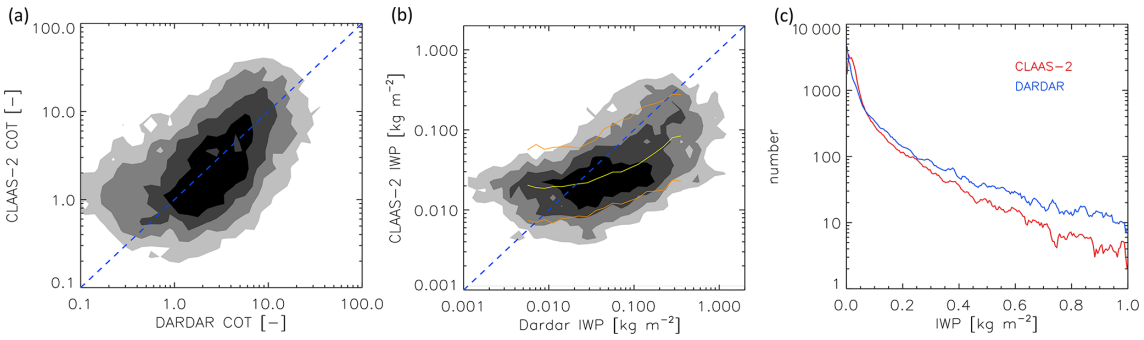

Figure 6. **(a)** Ice COT distribution comparing the collocated values retrieved from DARDAR and CLAAS-2. The blue dashed line is the 1 : 1 line and the gray scales indicate the regions enclosing 20, 40, 60 and 75 % of all data points. **(b)** As in **(a)** for the IWP. The yellow line depicts the median and the orange lines represent the 16th and 84th percentiles of the CLAAS-2 distribution at the corresponding DARDAR IWP. **(c)** 1-D histogram of DARDAR and CLAAS-2 IWP for the same collocations.

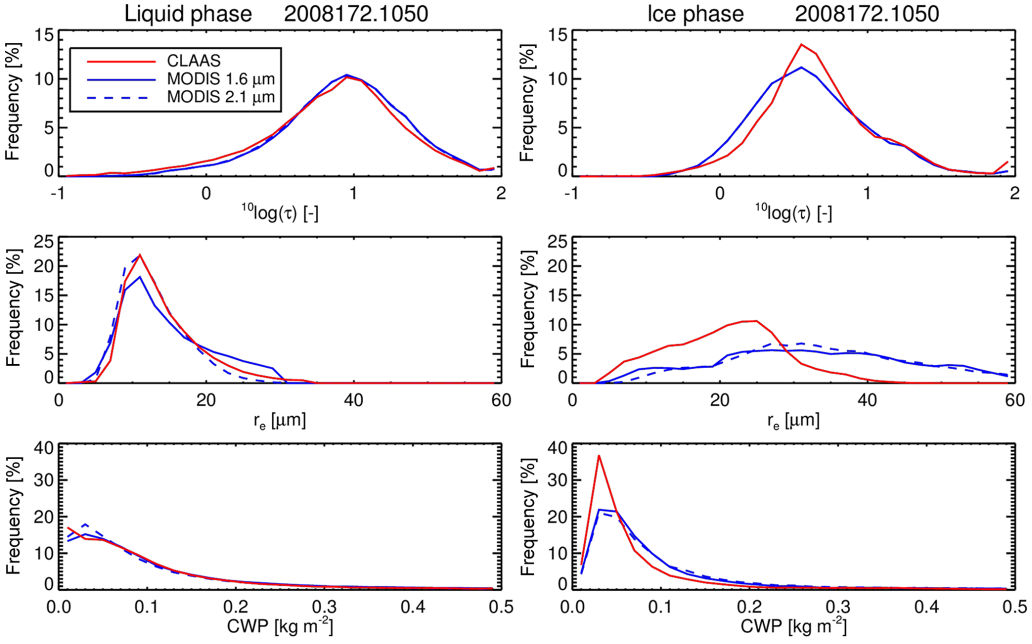

Figure 7. Histograms of CLAAS-2 and MODIS COT (top), REF (middle) and CWP (bottom) for the selected MODIS granule on 20 June 2008. The left panels are liquid clouds and the right panels are ice clouds. Only pixels for which both products agree on CPH are included. For MODIS the standard and PCL (partly cloudy) retrievals were combined, and results are shown for retrievals with two different wavelength bands (1.6 and 2.1 µm). Note that differences between MODIS 1.6 and 2.1 µm based on COT are small. Hence, the solid and dashed blue lines in the top panels cannot be distinguished.

increase that may be a retrieval artifact related to illumination geometry (high SZAs).

5.3 Comparison with MODIS

Figure 10 shows the intercomparison of CLAAS-2 and MODIS level 3 spatial distributions computed by averaging monthly data from the entire CLAAS-2 period, along with their differences. In the CFC and CPH cases (Fig. 10a and c), MODIS data are based on the cloud mask product, which is affected by the Terra calibration drift issue. Hence, an intercomparison only with Aqua MODIS data was performed in these two cases, as described in Sect. 3.3.

The two datasets have similar CFC spatial patterns (Fig. 10a), with lower values from CLAAS-2 appearing over central and western Africa and higher towards the edge of the disk. This pattern of differences should probably be attributed to the viewing geometry of SEVIRI with increasing viewing angles from the nadir of Meteosat to the edges of the SEVIRI disk, which would also lead to increased cloud cover retrieval compared to the MODIS typical range of viewing angles (Fig. 2). In addition, the difference tends to have an

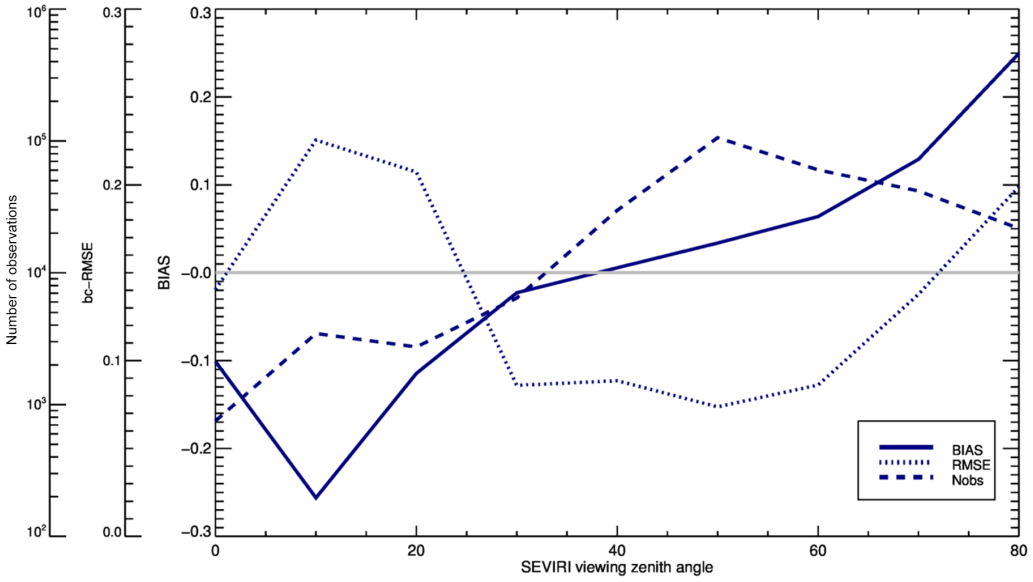

Figure 8. Dependency of the level 3 CLAAS-2–SYNOP CFC bias, bc-RMSE and SYNOP number of observations on the SEVIRI viewing zenith angle.

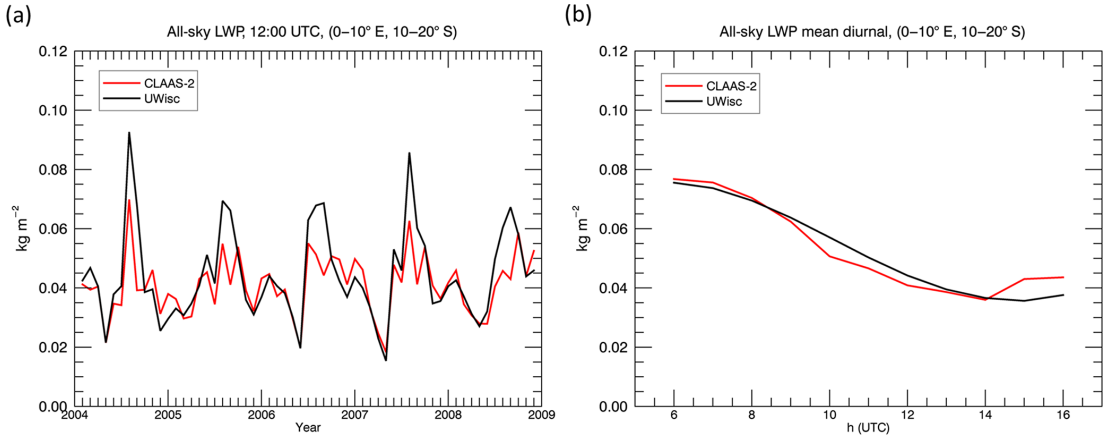

Figure 9. **(a)** Time series of the monthly all-sky LWP over the marine Sc region (0–10° E, 10–20° S) at 12:00 UTC from CLAAS-2 and UWisc data. **(b)** Monthly mean diurnal cycle of all-sky LWP from CLAAS-2 and UWisc over the same region.

opposite sign over land and ocean that is most pronounced e.g., over South America, Europe and the Red Sea. Figure 10b shows the CTH distributions and differences. Overall, CLAAS-2 tends to estimate higher cloud top heights, with the exceptions of central Africa and the Sahara where for the latter region CFC is minimal. The southern Atlantic marine Sc clouds are also placed slightly lower in CLAAS-2. The fraction of liquid clouds, expressed in CPH, is shown in Fig. 10c. As expected, the patterns are similar to the CTH case, with liquid clouds clearly prevailing at lower CTHs. Compared to MODIS, CLAAS-2 retrieves more ice clouds at the eastern and western edges of the disk and more liquid clouds around the 60° S zone. Figure 10d shows the spatial distribution of the all-sky LWP from CLAAS-2 and MODIS and their differences. In both datasets, high all-sky LWP values appear mainly over the southern and northern Atlantic and Europe, while the Sc region west of southern Africa is also highlighted. In terms of differences, there is an overall tendency for opposite signs over land and ocean, as in the CFC case. The all-sky IWP spatial distribution depicted in Fig. 10e reveals good agreement in terms of spatial features between CLAAS-2 and MODIS, with high values over central Africa, the Intertropical Convergence Zone (ITCZ) and South America. Similar patterns appear in the differences map, suggesting a proportionality to the absolute all-sky IWP values. CLAAS-2 generally acquires lower values than MODIS, with a few exceptions near Antarctica where sea ice might be causing artifacts in the CLAAS-2 retrieval.

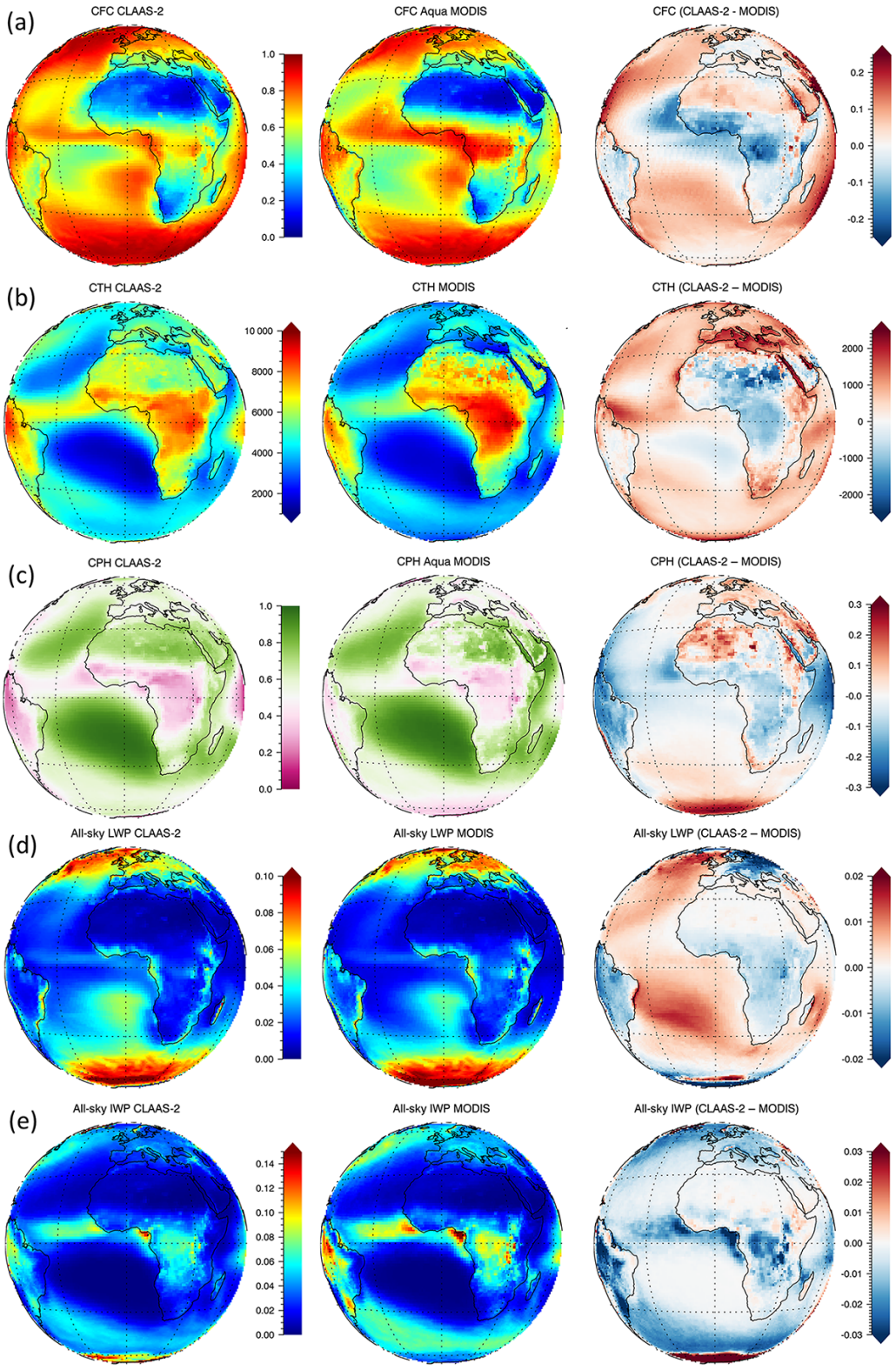

Figure 10. Spatial distributions of CFC **(a)**, CTH **(b)**, CPH (liquid cloud fraction) **(c)**, all-sky LWP **(d)** and all-sky IWP **(e)** averaged from February 2004 until December 2015 from CLAAS-2 (left column) and MODIS (middle column). The right column shows the corresponding differences. Aqua MODIS data were used in **(a)** and **(c)**; average Aqua and Terra MODIS data were used in **(b)**, **(d)** and **(e)**. Units are 1 **(a, c)**, m **(b)** and kg m^{-2} **(d, e)**.

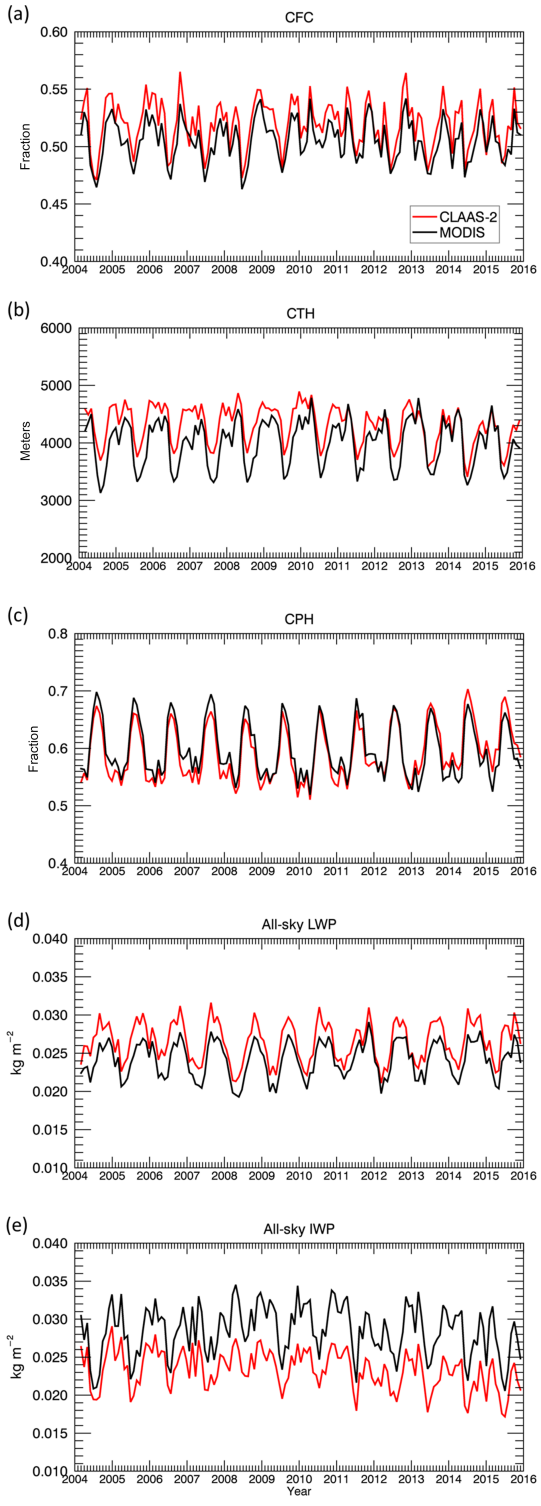

Figure 11. Time series of the 45° W–E and S–N area-averaged CFC **(a)**, CTH **(b)**, CPH (liquid cloud fraction) **(c)**, all-sky LWP **(d)** and all-sky IWP **(e)** from CLAAS-2 and MODIS. Aqua MODIS data were used in **(a)** and **(c)**; average Aqua and Terra MODIS data were used in **(b)**, **(d)** and **(e)**.

The lower CLAAS-2 IWP is consistent with the level-2 comparisons in Fig. 7, demonstrating that it is mainly explained by differences in the effective radius retrievals.

Overall, the intercomparison of temporally averaged distributions shows that CLAAS-2 and MODIS are in good agreement. In all the variables shown in Fig. 10, additional possible reasons causing differences between the datasets include the diurnal variability in clouds, which is not fully captured by MODIS, differences in cloud masking algorithms and the spatial averaging processes being used for the production of level 3 data.

Figure 11 shows the time series of the area-weighted averages of CLAAS-2 and MODIS level 3 cloud products over the 45° W–E and S–N region. This area was selected instead of the entire SEVIRI disk to ensure consistency in the time series of the daytime products in all seasons.

The daytime CFC time series (Fig. 11a) shows that CLAAS-2 and MODIS are in good agreement regarding both seasonal cycle and absolute values, also considering their differences in temporal sampling (averaging of daytime versus once-per-day retrievals). Both time series also appear stable throughout the 12-year period examined with no significant trend. The tendency of CLAAS-2 to acquire higher CTH values compared to MODIS, as presented in Fig. 10b, is verified by the corresponding time series (Fig. 11b); while the seasonality of CTH is similar in both data records, the mean CTH difference between them is ~ 300 m. It is worth noting, however, that this difference decreases after 2013 due to a slight decrease in CLAAS-2 CTH. This change, not appearing in MODIS data, should probably be attributed to the transition from MSG-2 to MSG-3 that occurred in January 2013, but further investigation is required to confirm this. A similar feature appears in the CPH time series (Fig. 11c), with very good agreement in terms of seasonal variation and absolute values and a transition of CLAAS-2 from slightly lower to slightly higher values compared to MODIS in 2013. The CLAAS-2 monthly all-sky LWP is systematically higher than MODIS by $0.002\,\mathrm{kg\,m^{-2}}$ on average (Fig. 11d). This should be attributed to the positive differences over the Atlantic Ocean, which covers a large part of the 45° W–E and S–N region. Furthermore, no significant change or trend appears in either dataset. This is not the case, however, in the all-sky IWP; in both CLAAS-2 and MODIS a decreasing trend appears during the second half of the time series (Fig. 11e). While further investigation of this feature is beyond the scope of this study, its presence and consistency in both data records suggests an origin beyond sensor or calibration issues. The mean difference between the two datasets is around $-0.005\,\mathrm{kg\,m^{-2}}$ throughout the time series.

6 Data availability

The CM SAF CLAAS-2 data record is freely available at https://doi.org/10.5676/EUM_SAF_CM/CLAAS/V002. The site provides documentation, related publications and links to auxiliary data, further data record details and ordering.

7 Summary

This study focused on the validation and intercomparison of the recently released cloud property data record CLAAS-2 by CM SAF based on measurements from the SEVIRI sensor onboard the geostationary satellites MSG-1, 2 and 3. The main characteristics of the retrieval algorithms used for the creation of CLAAS-2 were described, along with their updates compared to the first CLAAS edition.

A variety of reference datasets from different sensors and based on different retrieval approaches were used to evaluate and intercompare the CLAAS-2 retrievals at all possible processing levels. Validation was based on active sensors, which are considered the most accurate measurements of cloud properties in the atmosphere, and on ground-based observations. Intercomparisons were made with MODIS, which is one of the most advanced passive sensors with retrievals similar to those used in CLAAS-2.

The results revealed overall good agreement between CLAAS-2 and the reference datasets. While no major discrepancies were found, the differences reported can be attributed to various factors ranging from different retrieval approaches (e.g., profile retrievals from active sensors versus column-integrated retrievals from passive sensors), different microphysical assumptions in otherwise similar methodologies (e.g., between CLAAS-2 and MODIS) and differences in spatial and temporal samplings and viewing geometries. Considering all these factors, the results presented here confirm the reliability and stability of CLAAS-2 data.

In view of the present findings, CLAAS-2 can be considered a valuable source of data for studies on clouds and their role in the (regional) climate system. By making use of the advantages of a geostationary imager, it combines high spatial and temporal resolutions, rendering the data products suitable for both local- and continental-scale studies at time frames ranging from sub-hourly processes to interannual variability.

Recently, EUMETSAT and the co-funding national meteorological services secured the continuation of this work, and a third edition of CLAAS is planned for release around 2021, which will benefit from potentially improved calibration, further enhanced retrievals schemes and prolonged time coverage.

Appendix A: List of abbreviations

AMSR-E	Advanced Microwave Scanning Radiometer for Earth Observing System
AVHRR	Advanced Very High-Resolution Radiometer
bc-RMSE	Bias-corrected root mean square error
CALIOP	Cloud-Aerosol Lidar with Orthogonal Polarization
CALIPSO	Cloud-Aerosol Lidar and Infrared Pathfinder Satellite Observation
CDR	Climate data record
CFC	Cloud fractional coverage
CLAAS	Cloud property dAtAset using SEVIRI
CLARA	CM SAF cLoud, Albedo and surface RAdiation dataset
CM SAF	Satellite Application Facility on Climate Monitoring
COT	Cloud optical thickness
CPH	Cloud phase
CPP	Cloud Physical Properties
CPR	Cloud Profiling Radar
CTH	Cloud top height
CTP	Cloud top pressure
CTT	Cloud top temperature
CWP	Cloud water path
DAK	Doubling–Adding KNMI
DARDAR	raDAR–liDAR
ERA-Interim	ECMWF Reanalysis Interim Dataset
ECMWF	European Centre for Medium-Range Weather Forecasts
EUMETSAT	European Organisation for the Exploitation of Meteorological Satellites
FAR	False alarm ratio
GCOS	Global Climate Observing System
HRV	High Spatial Resolution Visible Channel
ICOT	Integrated COT
IPCC	Intergovernmental Panel on Climate Change
IR	Infrared
ISCCP	International Satellite Cloud Climatology Project
ITCZ	Intertropical Convergence Zone
IWP	Ice water path
KSS	Hanssen–Kuiper skill score
LUT	Lookup table
LWP	Liquid water path
MODIS	Moderate Resolution Imaging Spectroradiometer
MODTRAN	Moderate Resolution Atmospheric Transmission
MSG	Meteosat Second Generation
MW	Microwave
NASA	National Aeronautics and Space Administration
NESDIS	NOAA Satellite and Information Service
NOAA	National Oceanic and Atmospheric Administration
NWC SAF	Nowcasting and Very Short Range Forecasting Satellite Application Facility
OSI SAF	Ocean and Sea Ice Satellite Application Facility
PATMOS-x	Pathfinder Atmospheres-Extended
POD	Probability of detection
REF	Effective radius
RTTOV	Radiative Transfer for TOVS
SEVIRI	Spinning Enhanced Visible and Infrared Imager
SSM/I	Special Sensor Microwave Imager
STAR	Center for Satellite Applications and Research
SYNOP	Surface synoptic observations
SZA	Solar zenith angle
TOA	Top-of-atmosphere
TOVS	TIROS Operational Vertical Sounder
TRMM	Tropical Rainfall Measuring Mission
UWisc	University of Wisconsin
VIS	Visible
VZA	Viewing zenith angle

Appendix B: Spectral characteristics of SEVIRI channels

Table B1. MSG SEVIRI channels. Specifications include channel number, central wavelength (μm) and nominal spectral bandwidth (μm).

Channel	Central wavelength	Spectral bandwidth
HRV	n/a	About 0.4–1.1
1	0.635	0.56–0.71
2	0.81	0.74–0.88
3	1.64	1.50–1.78
4	3.92	3.48–4.36
5	6.25	5.35–7.15
6	7.35	6.85–7.85
7	8.70	8.30–9.10
8	9.66	9.38–9.94
9	10.80	9.80–11.80
10	12.00	11.00–13.00
11	13.40	12.40–14.40

n/a = not applicable

Competing interests. The authors declare that they have no conflict of interest.

Acknowledgements. The authors thank Andrew Heidinger (NOAA) for the provision of the modified version of the Pavolonis et al. (2005) cloud phase algorithm.

This work was performed within CM SAF funded by EUMETSAT in cooperation with the national meteorological services of Germany, Sweden, Finland, the Netherlands, Belgium, Switzerland and the United Kingdom.

Edited by: Alexander Kokhanovsky
Reviewed by: two anonymous referees

References

Alexandri, G., Georgoulias, A. K., Zanis, P., Katragkou, E., Tsikerdekis, A., Kourtidis, K., and Meleti, C.: On the ability of RegCM4 regional climate model to simulate surface solar radiation patterns over Europe: an assessment using satellite-based observations, Atmos. Chem. Phys., 15, 13195–13216, https://doi.org/10.5194/acp-15-13195-2015, 2015.

Anderson, G. P., Berk, A., Acharya, P. K., Matthew, M. W., Bernstein, L. S., Chetwynd, J. H., Dothe, H., Adler-Golder, S. M., Ratkowski, A. J., Felde, G. W., Gardner, J. A., Hoke, M. L., Richtsmeier, S. C., and Jeong, L. S.: MODTRAN4 version 2: radiative transfer modeling, P. SPIE, 4381, 455–459, 2001.

Baum, B. A., Menzel, W. P., Frey, R. A., Tobin, D. C., Holz, R. E., Ackerman, S. A., Heidinger, A. K., and Yang, P.: MODIS Cloud-Top Property Refinements for Collection 6, J. Appl. Meteorol. Clim., 51, 1145–1163, https://doi.org/10.1175/JAMC-D-11-0203.1, 2012.

Brisson, E., Van Weverberg, K., Demuzere, M., Devis, A., Saeed, S., Stengel, M., and Van Lipzig, N. P. M.: How well can a convection-permitting climate model reproduce decadal statistics of precipitation, temperature and cloud characteristics?, Clim. Dynam., 47, 3043–3061, https://doi.org/10.1007/s00382-016-3012-z, 2016.

CM SAF: Algorithm Theoretical Basis Document, SEVIRI cloud products, CLAAS Edition 2, EUMETSAT Satellite Application Facility on Climate Monitoring, SAF/CM/DWD/ATBD/SEV/CLD, Issue 2, Rev. 3, https://doi.org/10.5676/EUM_SAF_CM/CLAAS/V002, 17 June 2016a.

CM SAF: Algorithm Theoretical Basis Document, SEVIRI Cloud Physical Products, CLAAS Edition 2, EUMETSAT Satellite Application Facility on Climate Monitoring, SAF/CM/KNMI/ATBD/SEVIRI/CPP, Issue 2, Rev. 2, https://doi.org/10.5676/EUM_SAF_CM/CLAAS/V002, 10 June 2016b.

de Graaf, M., Tilstra, L. G., Wang, P., and Stammes, P.: Retrieval of the aerosol direct radiative effect over clouds from spaceborne spectrometry, J. Geophys. Res., 117, D07207, https://doi.org/10.1029/2011JD017160, 2012.

Dee, D. P., Uppala, S. M., Simmons, A. J., Berrisford, P., Poli, P., Kobayashi, S., Andrae, U., Balmaseda, M. A., Balsamo, G., Bauer, P., Bechtold, P., Beljaars, A. C. M., van de Berg, L., Bidlot, J., Bormann, N., Delsol, C., Dragani, R., Fuentes, M., Geer, A. J., Haimberger, L., Healy, S. B., Hersbach, H., Hólm, E. V., Isaksen, L., Kallberg, P., Köhler, M., Matricardi, M., McNally, A. P., Monge-Sanz, B. M., Morcrette, J.-J., Park, B.-K., Peubey, C., de Rosnay, P., Tavolato, C., Thépaut, J.-N., and Vitart, F.: The ERA-Interim reanalysis: configuration and performance of the data assimilation system, Q. J. Roy. Meteor. Soc., 137, 553–597, 2011.

Delanoë, J. and Hogan, R. J.: A variational scheme for retrieving ice cloud properties from combined radar, lidar, and infrared radiometer, J. Geophys. Res., 113, D07204, https://doi.org/10.1029/2007JD009000, 2008.

Delanoë, J. and Hogan, R. J.: Combined CloudSat-CALIPSO-MODIS retrievals of the properties of ice clouds, J. Geophys. Res., 115, D00H29, https://doi.org/10.1029/2009JD012346, 2010.

Derrien, M. and Le Gléau, H.: MSG/SEVIRI cloud mask and type from SAFNWC, Int. J. Remote Sens., 26, 4707–4732, 2005.

Eliasson, S., Holl, G., Buehler, S. A., Kuhn, T., Stengel, M., Iturbide-Sanchez, F., and Johnston, M.: Systematic and random errors between collocated satellite ice water path observations, J. Geophys. Res.-Atmos., 118, 2629–2642, https://doi.org/10.1029/2012JD018381, 2013.

Finkensieper, S., Meirink, J. F., van Zadelhoff, G.-J., Hanschmann, T., Benas, N., Stengel, M., Fuchs, P., Hollmann, R., and Werscheck, M.: CLAAS-2: CM SAF CLoud property dAtAset using SEVIRI – Edition 2. Satellite Application Facility on Climate Monitoring, https://doi.org/10.5676/EUM_SAF_CM/CLAAS/V002, 2016.

Haywood, J. M., Osborne, S. R., and Abel, S. J.: The effect of overlying absorbing aerosol layers on remote sensing retrievals of cloud effective radius and cloud optical depth, Q. J. Roy. Meteor. Soc., 130, 779–800, 2004.

Heidinger, A. K., Foster, M. J., Walther, A., and Zhao, X.: The Pathfinder Atmospheres Extended (PATMOS-x) AVHRR climate data set, B. Am. Meteorol. Soc., 95, https://doi.org/10.1175/BAMS-D-12-00246.1, 2014.

Hess, M., Koelemeijer, R. B. A., and Stammes, P.: Scattering matrices of imperfect hexagonal ice crystals, J. Quant. Spectrosc. Ra., 60, 301–308, 1998.

Jarraud, M.: Guide to Meteorological Instruments and Methods of Observation (WMO – No. 8), World Meteorological Organisation, Geneva, Switzerland, 2008.

Karlsson, K.-G.: A ten-year cloud climatology over Scandinavia derived from NOAA AVHRR imagery, Int. J. Climatol., 23, 1023–1044, https://doi.org/10.1002/joc.916, 2003.

Karlsson, K.-G., Riihelä, A., Müller, R., Meirink, J. F., Sedlar, J., Stengel, M., Lockhoff, M., Trentmann, J., Kaspar, F., Hollmann, R., and Wolters, E.: CLARA-A1: a cloud, albedo, and radiation dataset from 28 yr of global AVHRR data, Atmos. Chem. Phys., 13, 5351–5367, https://doi.org/10.5194/acp-13-5351-2013, 2013.

Karlsson, K.-G., Anttila, K., Trentmann, J., Stengel, M., Fokke Meirink, J., Devasthale, A., Hanschmann, T., Kothe, S., Jääskeläinen, E., Sedlar, J., Benas, N., van Zadelhoff, G.-J., Schlundt, C., Stein, D., Finkensieper, S., Håkansson, N., and Hollmann, R.: CLARA-A2: the second edition of the CM SAF cloud and radiation data record from 34 years of

global AVHRR data, Atmos. Chem. Phys., 17, 5809–5828, https://doi.org/10.5194/acp-17-5809-2017, 2017.

Knap, W. H., Labonnote, L. C., Brogniez, G., and Stammes, P.: Modeling total and polarized reflectances of ice clouds: evaluation by means of POLDER and ATSR-2 measurements, Appl. Optics, 44, 4060–4073, 2005.

Maddux, B. C., Ackerman, S. A., and Platnick, S.: Viewing Geometry Dependencies in MODIS Cloud Products, J. Atmos. Ocean. Tech., 27, 1519–1528, https://doi.org/10.1175/2010JTECHA1432.1, 2010.

Martins, J. P. A., Cardoso, R. M., Soares, P. M. M., Trigo, I. F., Belo-Pereira, M., Moreira, N., and Tomé, R.: The summer diurnal cycle of coastal cloudiness over west Iberia using Meteosat/SEVIRI and a WRF regional climate model simulation, Int. J. Climatol., 36, 1755–1772, https://doi.org/10.1002/joc.4457, 2016.

Matricardi, M., Chevallier, F., Kelly, G., and Thepaut, J.-N.: An improved general fast radiative transfer model for the assimilation of radiance observations, Q. J. Roy. Meteor. Soc., 130, 153–173, https://doi.org/10.1256/qj.02.181, 2004.

Meirink, J. F., Roebeling, R. A., and Stammes, P.: Inter-calibration of polar imager solar channels using SEVIRI, Atmos. Meas. Tech., 6, 2495–2508, https://doi.org/10.5194/amt-6-2495-2013, 2013.

Menzel, W. P., Smith, W. L., and Stewart, T. R.: Improved Cloud Motion Wind Vector and Altitude Assignment using VAS, J. Appl. Meteorol. Clim., 22, 377–384, 1983.

Moody, E. G., King, M. D., Platnick, S., Schaaf, C. B., and Gao, F.: Spatially complete global spectral surface albedos: value-added datasets derived from Terra MODIS land products, IEEE T. Geosci. Remote S., 43, 144–158, 2005.

Nakajima, T. and King, M. D.: Determination of the optical thickness and effective particle radius of clouds from reflected solar radiation measurements, part 1: Theory, J. Atmos. Sci., 47, 1878–1893, 1990.

NWC SAF: Scientific report on improving "Cloud Products" (CMa-PGE01 v3.1, CT-PGE02 v2.1 & CTTH-PGE03 v2.2), EUMETSAT Satellite Application Facility on Nowcasting and Short range Forecasting, SAF/NWC/CDOP/MFL/SCI/RP/06, Issue 1, Rev. 0, 24 March 2011.

NWC SAF: Algorithm Theoretical Basis Document for "Cloud Products" (CMa-PGE01 v3.2, CT-PGE02 v2.2 and CTTH-PGE03 v2.2), EUMETSAT Satellite Application Facility on Nowcasting and Short range Forecasting, SAF/NWC/CDOP2/MFL/SCI/ATBD/01, Issue 3, Rev. 2.1, 15 July 2013.

O'Dell, C. W., Wentz, F. J., and Bennartz, R.: Cloud liquid water path from satellite-based passive microwave observations: a new climatology over the global oceans, J. Climate, 21, 1721–1739, 2008.

OSI SAF: The EUMETSAT OSI SAF Sea Ice Concentration Algorithm. Algorithm Theoretical Basis Document, SAF/OSI/CDOP/DMI/SCI/MA/189, Version 1.5, 2016.

Pavolonis, M. J., Heidinger, A. K., and Uttal, T.: Daytime global cloud typing from AVHRR and VIIRS: Algorithm description, validation, and comparison, J. Appl. Meteorol., 44, 804–826, https://doi.org/10.1175/JAM2236.1, 2005.

Pfeifroth, U., Trentmann, J., Fink, A., and Ahrens, B.: Evaluating Satellite-Based Diurnal Cycles of Precipitation in the African Tropics, J. Appl. Meteorol. Clim., 55, 23–39, https://doi.org/10.1175/JAMC-D-15-0065.1, 2016.

Platnick, S., King, M. D., Meyer, K. G., Wind, G., Amarasinghe, N., Marchant, B., Arnold, G. T., Zhang, Z., Hubanks, P. A., Ridgway, B., and Riédi, J.: MODIS Cloud Optical Properties: User Guide for the Collection 6 Level-2 MOD06/MYD06 Product and Associated Level-3 Datasets, Version 1.0, available at http://modis-atmos.gsfc.nasa.gov/_docs/C6MOD06OPUserGuide.pdf (last access: 31 May 2016), 2015.

Platnick, S. E., King, M. D., Ackerman, S. A., Menzel, W. P., Baum, B. A., Riédi, J. C., and Frey, R. A.: The MODIS cloud products: Algorithms and examples from Terra, IEEE T. Geosci. Remote S., 41, 459–473, 2003.

Reuter, M., Thomas,W., Albert, P., Lockhoff, M.,Weber, R., Karlsson, K.-G., and Fischer, J.: The CM-SAF and FUB Cloud Detection Schemes for SEVIRI: Validation with Synoptic Data and Initial Comparison with MODIS and CALIPSO, J. Appl. Meteorol. Clim., 48, 301–316, https://doi.org/10.1175/2008JAMC1982.1, 2009.

Roebeling, R. A., Feijt, A. J., and Stammes, P.: Cloud property retrievals for climate monitoring: implications of differences between SEVIRI on METEOSAT-8 and AVHRR on NOAA-17, J. Geophys. Res., 111, D20210, https://doi.org/10.1029/2005JD006990, 2006.

Rossow, W. B. and Schiffer, R. A.: Advances in understanding clouds from ISCCP, B. Am. Meteorol. Soc., 80, 2261–2287, 1999.

Salomonson, V. V., Barnes, W. L., Maymon, P. W., Montgomery, H. E., and Ostrow, H.: MODIS: Advanced facility instrument for studies of the earth as a system, IEEE T. Geosci. Remote S., 27, 145–153, https://doi.org/10.1109/36.20292, 1989.

Saunders, R., Matricardi, M., and Brunel, P.: An improved fast radiative transfer model for assimilation of satellite radiance observations, Q. J. Roy. Meteor. Soc., 125, 1407–1425, https://doi.org/10.1002/qj.1999.49712555615, 1999.

Schmetz, J., Holmlund, K., Hoffman, J., Strauss, B., Mason, B., Gaertner, V., Koch, A., and Van De Berg, L.: Operational cloud motion winds from Meteosat infrared images, J. Appl. Meteorol., 32, 1206–1225, 1993.

Schulz, J., Albert, P., Behr, H.-D., Caprion, D., Deneke, H., Dewitte, S., Dürr, B., Fuchs, P., Gratzki, A., Hechler, P., Hollmann, R., Johnston, S., Karlsson, K.-G., Manninen, T., Müller, R., Reuter, M., Riihelä, A., Roebeling, R., Selbach, N., Tetzlaff, A., Thomas, W., Werscheck, M., Wolters, E., and Zelenka, A.: Operational climate monitoring from space: the EUMETSAT Satellite Application Facility on Climate Monitoring (CM-SAF), Atmos. Chem. Phys., 9, 1687–1709, https://doi.org/10.5194/acp-9-1687-2009, 2009.

Segelstein, D.: The complex refractive index of water, MSc Thesis, University of Missouri, Kansas City, 1981.

Stammes, P.: Spectral radiance modelling in the UV-Visible range, in: IRS 2000: Current problems in Atmospheric Radiation, edited by: Smith, W. L. and Timofeyev, Y. M. A., Deepak, Hampton, VA, 385–388, 2001.

Stengel, M., Kniffka, A., Meirink, J. F., Lockhoff, M., Tan, J., and Hollmann, R.: CLAAS: the CM SAF cloud property data set using SEVIRI, Atmos. Chem. Phys., 14, 4297–4311, https://doi.org/10.5194/acp-14-4297-2014, 2014.

Stephens, G.: Radiation profiles in extended water clouds, II: Parameterization schemes, J. Atmos. Sci., 35, 2123–2132, 1978.

Stocker, T. F., Qin, D., Plattner, G.-K., Tignor, M., Allen, S. K., Boschung, J., Nauels, A., Xia, Y., Bex, V., and Midgley, P. (Eds.): Climate Change 2013: The physical science basis. Contribution of Working Group I to the Fifth Assessment Report of the Intergovernmental Panel on Climate Change, Cambridge University Press, Cambridge, United Kingdom and New York, NY, USA, 2013.

Sun, W., Videen, G., Kato, S., Lin, B., Lukashin, C., and Hu, Y.: A study of subvisual clouds and their radiation effect with a synergy of CERES, MODIS, CALIPSO and AIRS data, J. Geophy. Res., 116, D22207, https://doi.org/10.1029/2011JD016422, 2011.

Tilstra, L. G., de Graaf, M., Aben, I., and Stammes, P.: In-flight degradation correction of SCIAMACHY UV reflectances and Absorbing Aerosol Index, J. Geophys. Res., 117, D06209, https://doi.org/10.1029/2011JD016957, 2012.

Warren, S. G. and Brandt, R. E.: Optical constants of ice from the ultraviolet to the microwave: A revised compilation, J. Geophys. Res., 113, D14220, https://doi.org/10.1029/2007JD009744, 2008.

Winker, D. M., Vaughan, M. A., Omar, A., Hu, Y., Powell, K. A., Liu, Z., Hunt, W. H., and Young, S. A.: Overview of the CALIPSO Mission and CALIOP data processing algorithms, J. Atmos. Ocean. Tech., 26, 2310–2323, https://doi.org/10.1175/2009JTECHA1281.1, 2009.

Wu, A., Xiong, X., Doelling, D. R., Morstad, D., Angal, A., and Bhatt, R.: Characterization of Terra and Aqua MODIS VIS, NIR, and SWIR spectral bands' calibration stability, IEEE T. Geosci. Remote S., 51, 4330–4338, 2013.

Yang, P., Bi, L., Baum, B. A., Liou, K. N., Kattawar, G. W., Mishchenko, M. I., and Cole, B.: Spectrally consistent scattering, absorption, and polarization properties of atmospheric ice crystals at wavelengths from 0.2 to 100 µm, J. Atmos. Sci., 70, 330–347, https://doi.org/10.1175/JAS-D-12-039.1, 2013.